

# Optical detection of the susceptibility tensor in two-dimensional crystals

**Zhemi Xu**

Università degli studi di Padova

**Davide Ferraro**

Università degli studi di Padova

**Annamaria Zaltron**

Università degli studi di Padova

**Nicola Galvanetto**

Università degli studi di Padova

**Alessandro Martucci**

Università degli studi di Padova <https://orcid.org/0000-0001-9601-8640>

**Luzhao Sun**

Peking University <https://orcid.org/0000-0003-0518-0744>

**Pengfei Yang**

Peking University

**Yanfeng Zhang**

Peking University <https://orcid.org/0000-0003-1319-3270>

**Yuechen Wang**

Peking University

**Zhongfan Liu**

Peking University <https://orcid.org/0000-0001-5554-1902>

**Joshua Elliott**

University of Manchester

**Margherita Marsili**

Università degli studi di Padova

**Luca dell'Anna**

Università degli studi di Padova

**Paolo Umari**

Università degli studi di Padova

**Michele Merano** (✉ [michele.merano@unipd.it](mailto:michele.merano@unipd.it))

Università degli studi di Padova

**Keywords:** out-of-plane optical constants, two-dimensional materials, photonics, optoelectronics

**Posted Date:** March 18th, 2021

**DOI:** <https://doi.org/10.21203/rs.3.rs-266618/v1>

**License:**  This work is licensed under a Creative Commons Attribution 4.0 International License.

[Read Full License](#)

---

**Version of Record:** A version of this preprint was published at Communications Physics on September 23rd, 2021. See the published version at <https://doi.org/10.1038/s42005-021-00711-3>.

1 *Optical detection of the susceptibility tensor in two-dimensional*  
2 *crystals*

3 **Zhemi Xu<sup>1,2</sup>, Davide Ferraro<sup>1</sup>, Annamaria Zaltron<sup>1</sup>, Nicola Galvanetto<sup>1</sup>, Alessandro Martucci<sup>3</sup>, Luzhao**  
4 **Sun<sup>4,5</sup>, Pengfei Yang<sup>6</sup>, Yanfeng Zhang<sup>6</sup>, Yuechen Wang<sup>4,5</sup>, Zhongfan Liu<sup>4,5</sup>, Joshua D. Elliott<sup>7</sup>, Margherita**  
5 **Marsili<sup>1</sup>, Luca Dell’Anna<sup>1</sup>, Paolo Umari<sup>1</sup> & Michele Merano<sup>1</sup>✉**

6 <sup>1</sup>Dipartimento di Fisica e Astronomia “Galileo Galilei”, Università degli Studi di Padova, via Marzolo 8, I-  
7 35131, Padova Italy.

8 <sup>2</sup>College of Chemistry and Materials Engineering, Beijing Technology and Business University, Beijing,  
9 100048, P. R. China.

10 <sup>3</sup>Dipartimento di Ingegneria Industriale, Università degli Studi di Padova, via Marzolo 9, I-35131, Padova  
11 Italy.

12 <sup>4</sup>Center for Nanochemistry, Beijing Science and Engineering Center for Nanocarbons, Beijing National  
13 Laboratory for Molecular Sciences, College of Chemistry and Molecular Engineering, Peking University,  
14 Beijing 100871, P. R. China.

15 <sup>5</sup>Beijing Graphene Institute, Beijing 100095, P. R. China.

16 <sup>6</sup>Academy for Advanced Interdisciplinary Studies, College of Engineering, Peking University, Beijing  
17 100871, People’s Republic of China.

18 <sup>7</sup>Department of Chemical Engineering and Analytical Science, University of Manchester, Manchester M13  
19 9PL, United Kingdom

20 ✉e-mail: michele.merano@unipd.it

21 **The out-of-plane optical constants of two-dimensional materials have proven to be experimentally**  
22 **elusive. Owing to the reduced dimensionality of a monolayer, optical measurements have limited**  
23 **sensitivity to these properties, which are hidden by the optical response of the substrate<sup>1</sup>. Therefore,**  
24 **there remains an absence of scientific consensus on how to correctly model these materials<sup>2-7</sup>.**  
25 **Theoretical descriptions span from isotropic three-dimensional slabs<sup>6-9</sup> to two-dimensional surface**  
26 **currents with a null out-of-plane surface susceptibility<sup>2,5,10-12</sup>. Here we perform a smoking gun**  
27 **experiment on the optical response of a single-layer two-dimensional crystal that addresses these**

28 **problems. We successfully remove the substrate contribution to the optical response of these materials**  
29 **by a step deposition of a monolayer crystal inside a thick polydimethylsiloxane prism. This allows for a**  
30 **reliable determination of both the in-plane and the out-of-plane components of the monolayer surface**  
31 **susceptibility tensor. Our results prescribe one clear theoretical model for these types of material. This**  
32 **work creates opportunities for a precise characterization of the optical properties of two-dimensional**  
33 **crystals in all the optical domains such as the nonlinear response<sup>13</sup>, surface wave phenomena<sup>14</sup> or**  
34 **magneto-optical Kerr effect<sup>15</sup>. Our assay will be relevant to future progresses in photonics and**  
35 **optoelectronics with 2D materials<sup>16,17</sup>.**

36 One of the great achievements in materials science is certainly the isolation of individual crystal planes,  
37 starting from solids with strong in-plane bonds and weak, van der Waals-like, coupling between layers. In  
38 general, when dealing with layered crystals, Maxwell's equations increase in complexity in order to  
39 account for anisotropy. The susceptibility of these materials is no longer described by a constant, but by  
40 a tensor and, as regards to the optical properties, they are at least uniaxial. Consequently, we expect that  
41 the optical spectra of single-layer, two-dimensional (2D) crystals also show out-of-plane anisotropy. In  
42 spite of the fact that experimental assessment of the out-of-plane anisotropy for the three-dimensional  
43 crystal is manageable, this is not the case for isolated monolayers<sup>1</sup>. As a result, fifteen years after the  
44 exfoliation of the first atomically thin crystal, the exact description of its optical response remains an  
45 active and debated area of research<sup>2-7</sup>.

46 There are currently two main models in use for the optical description of single-layer crystals, the first is  
47 a thin film model that can be either isotropic or anisotropic along the vertical direction<sup>1,6-9,18</sup>. Optical  
48 contrast measurements, used to detect single and multiple layers of a 2D crystal, are analysed by choosing  
49 an isotropic thin film<sup>6,7,9</sup>. This is justified by the normal incidence configuration: the electric field is parallel  
50 to the crystal and the in-plane optical constants dominate the optical response. Surprisingly, the same

51 model applies to spectroscopic ellipsometry, a very sensitive technique that works at any angle of  
52 incidence. If the first ellipsometric data for graphene were fitted using a uniaxial thin film model<sup>18</sup>,  
53 subsequent analysis concluded that ellipsometry is only sensitive to the in-plane optical constants<sup>1</sup>. This  
54 because the sensitivity to anisotropy is dependent on the path length through the film, which is extremely  
55 limited for a monolayer<sup>1</sup>. We are aware of only two papers that claim a big difference in between optical  
56 constants of single-layer transition metal dichalcogenides (TMDC) extracted from ellipsometric data using  
57 an anisotropic and an isotropic thin film model<sup>19,20</sup>. However, the same articles also find large differences  
58 in the in-plane optical constants, a result in contradiction with several other works<sup>1,8,18,21,22</sup>.

59 In the second model, the monolayer is treated as a 2D surface current without any thickness. In this case,  
60 the system is intrinsically anisotropic with both null out-of-plane surface susceptibility ( $\chi_{\perp}$ ) and  
61 conductivity ( $\sigma_{\perp}$ )<sup>2,5,10-12</sup>. If on one side the use of two different models is a sign of a physical richness, on  
62 the other it poses new conundrums. The two approaches, starting from the measured ellipsometric  
63 parameters, provide a different in-plane surface susceptibility ( $\chi_{\parallel}$ ) and conductivity ( $\sigma_{\parallel}$ )<sup>21</sup>. For  $\chi_{\parallel}$ , this  
64 difference is greater than the experimental error<sup>21</sup>. From a theoretical point of view, the choice of setting  
65  $\chi_{\perp} = 0$  m and  $\sigma_{\perp} = 0 \Omega^{-1}$  in the surface current model is arbitrary, yet so is the use of an isotropic thin film  
66 model, when we expect the system to be highly anisotropic. Ab-initio many body calculation of the optical  
67 spectra of graphite, graphene and bilayer graphene report interesting differences in the simulated out-  
68 of-plane properties going from the bulk limit, down to a monolayer, but they exclude a null value<sup>23</sup>, this  
69 also holds for other 2D crystals like TMDC<sup>24</sup>.

70 One main experimental problem in the analysis of the optical response of a 2D crystal is the role of the  
71 substrate, that adds a background signal, hiding the small contribution that comes from the out-of-plane  
72 optical constants. We measure  $\chi_{\parallel}$ ,  $\sigma_{\parallel}$ ,  $\chi_{\perp}$  and  $\sigma_{\perp}$  in a two-step experiment (fig. 1 a, b). First, we extract the  
73 ellipsometric data ( $\Psi_s$ ,  $\Delta_s$ ) from a single-layer 2D crystal deposited on a transparent dielectric substrate,

74 namely polydimethylsiloxane (PDMS). Then, the same crystal is completely immersed in PDMS for a  
 75 second ellipsometric measurement that provides a new set of data ( $\Psi_s, \Delta_s$ ). By inverting the fundamental  
 76 equation of ellipsometry  $\tan \Psi e^{i\Delta} = r_p/r_s$ , where  $r_p$  and  $r_s$  are the Fresnel coefficients, it is possible to  
 77 extract  $\chi_{\parallel}, \sigma_{\parallel}, \chi_{\perp}, \sigma_{\perp}$  from  $\Psi_s, \Delta_s, \Psi_i, \Delta_i$ .

78 While the reflection coefficients for the anisotropic slab model are reported in ref.<sup>25</sup>, it is much more  
 79 difficult to find in the literature a complete and correct generalization of the surface current model to  
 80 include also the orthogonal polarization. We provide here the essential conceptual steps. The detailed  
 81 calculations of the Fresnel coefficients are in the Methods section. The polarization parallel  $\vec{P}_{\parallel}$  and  
 82 perpendicular  $\vec{P}_{\perp}$  to the crystal plane induce two surface currents:  $\vec{J}_{\parallel}$  and  $\vec{J}_{\perp}$  respectively. The reflected  
 83 field is the superposition of the reflected fields from these two currents. We thus solve two set of  
 84 boundary conditions<sup>26</sup>, one for  $\vec{J}_{\parallel}$ :

$$(1) \quad \hat{\kappa} \wedge (\vec{H}_2 - \vec{H}_1) = \frac{\partial \vec{P}_{\parallel}}{\partial t} = \vec{J}_{\parallel}$$

$$\hat{\kappa} \wedge (\vec{E}_2 - \vec{E}_1) = 0$$

85 and one for  $\vec{J}_{\perp}$ :

$$(2) \quad \hat{\kappa} \wedge (\vec{H}_2 - \vec{H}_1) = 0$$

$$\hat{\kappa} \wedge (\vec{E}_2 - \vec{E}_1) = -\frac{1}{\epsilon_0} \hat{\kappa} \wedge \text{grad}(P_{\perp}) = \vec{J}_{\perp}$$

86 Here  $\hat{k}, \hat{i}$  are the unitary vectors in the  $z$  and  $x$  direction (Fig. 1),  $\vec{H}$  is the magnetic field,  $\vec{E}$  the electric  
87 field,  $\epsilon_0$  the vacuum permittivity and the subscripts 1 and 2 refer to the media above and below the  
88 monolayer. The first set of boundary conditions are discussed in refs<sup>2,10,11</sup>, for the surface current model  
89 with null  $\vec{P}_\perp$ . The second set has the following simple explanation<sup>26-28</sup>. In the radiation zone<sup>29</sup>, the  
90 electromagnetic field due to an oscillating electric dipole in the  $\hat{k}$  direction is identical to an  
91 electromagnetic field due to an oscillating magnetic dipole in the  $-\hat{i}$  direction. This last one would cause  
92 a jump in the tangential component of  $\vec{E}$ .

93 Assuming a time dependence  $e^{i\omega t}$ , ( $\omega$  is the angular frequency of the light) for a monolayer completely  
94 immersed in a dielectric medium of refractive index  $n$  we find:

$$95 \quad (3) \quad r_{ip} = \frac{(ik\chi_{\parallel} + \sigma_{\parallel}\eta) \cos \theta}{(ik\chi_{\parallel} + \sigma_{\parallel}\eta) \cos \theta + 2n} - \frac{n(i k \chi_{\perp} + \sigma_{\perp}\eta) \tan \theta \sin \theta}{2 + n(i k \chi_{\perp} + \sigma_{\perp}\eta) \tan \theta \sin \theta}$$

96 where the subscript  $i$  denotes that the sample is immersed,  $p$  is in place of  $p$ -polarized light,  $k$  is the wave  
97 vector of light in vacuum,  $\eta$  is the impedance of vacuum and  $\theta$  is the angle of incidence. For a monolayer  
98 deposited at the interface of vacuum with a dielectric substrate of refractive index  $n$  we find:

$$99 \quad (4) \quad r_{sp} = -\frac{n \cos \theta - \cos \theta_t}{n \cos \theta + \cos \theta_t} + \frac{n \cos \theta - \cos \theta_t + (ik\chi_{\parallel} + \sigma_{\parallel}\eta) \cos \theta \cos \theta_t}{n \cos \theta + \cos \theta_t + (ik\chi_{\parallel} + \sigma_{\parallel}\eta) \cos \theta \cos \theta_t}$$

$$100 \quad + \frac{n^2 \cos \theta - n \cos \theta_t - (i k \chi_{\perp} + \sigma_{\perp}\eta) \sin^2 \theta}{n^2 \cos \theta + n \cos \theta_t + (i k \chi_{\perp} + \sigma_{\perp}\eta) \sin^2 \theta}$$

101 where the subscript  $s$  denotes the substrate, and  $\theta_t$  is the propagation angle in the dielectric. For  $s$   
102 polarized light the Fresnel coefficients depend only on  $\chi_{\parallel}, \sigma_{\parallel}$  and are provided in formula (6) of ref.<sup>2</sup>.

103 In our experiment, a 7x7 millimeter-size, polycrystalline, single-layer 2D crystal is deposited on a 1 cm  
104 thick (to avoid back reflections) PDMS substrate (2x2 cm square) by chemical vapor deposition (fig. 1a).

105 The first ellipsometric measurement (VASE ellipsometer, J. A. Wollam) provides  $\Psi_s$  and  $\Delta_s$  and the  
106 confirmation that we are dealing with a monolayer. We then place our sample in a prism-shaped mold  
107 (base 6x5 cm, height 3.5 cm), we pour non-polymerized PDMS on it and we wait for complete  
108 polymerization. This process successfully produces a 2D crystal immersed in PDMS without any additional  
109 interface in between the previous and the newly added material. The prism has two optical quality lateral  
110 windows (fig 1b). The light reflected by the sample in this second step is 2 orders of magnitude less than  
111 in the previous one, because there is no more the substrate contribution. For this reason, we set up a  
112 manual ellipsometer at the wavelength of 633 nm (fig. 1 c) to measure  $\Psi_i$  and  $\Delta_i$ .

113 We studied both monolayer graphene and MoS<sub>2</sub>. First, we tested our two steps procedure without  
114 deposition of the monolayer to ensure that we do not observe any reflection in between the embedded  
115 substrate and the final prism. Ellipsometric parameters  $\Psi_s$  and  $\Delta_s$  are measured at angles of incidence  $\theta_s$   
116 equal to 65° and 70° ( Figs 1 and 2 extended data section),  $\Psi_i$  and  $\Delta_i$  (figs 2a,b, 3a,b) are taken at angles  
117 of incidence  $\theta_i$  around the pseudo-Brewster angle, where  $\Delta_i$  varies appreciably and  $\Psi_i$  has a minimum.  
118 When  $\theta_i$  becomes too small,  $\Delta_i$  approaches 180° and noise becomes dominant.

119 Figures 2c,d, and 3c,d report the optical constants  $\chi_{\parallel}$ ,  $\sigma_{\parallel}$ ,  $\chi_{\perp}$ ,  $\sigma_{\perp}$  extracted from the ellipsometric data  
120 using the Fresnel coefficients provided by the anisotropic slab model (slab model) and by the surface  
121 current model (curr model). With no loss of information, for each  $\theta_i$  we report the average  $\chi_{\parallel}$ ,  $\sigma_{\parallel}$ ,  $\chi_{\perp}$ ,  $\sigma_{\perp}$   
122 considering the  $\Psi_s$ ,  $\Delta_s$  at 65° and 70°. The curr model gives a positive  $\chi_{\perp}$  while the slab model a negative  
123 one. Within our present experimental precision, we are not able to discriminate  $\sigma_{\perp}$  from zero and  $\chi_{\parallel}$ ,  $\sigma_{\parallel}$   
124 are similar. As usually done in the literature<sup>21</sup>, starting from the  $\Psi_s$  and  $\Delta_s$  (Figs. 1 and 2 extended data),  
125 the isotropic slab model (iso\_slab model) and the surface current model with null  $\chi_{\perp}$  and  $\sigma_{\perp}$  (curr\_0  
126 model) also furnish  $\chi_{\parallel}$  and  $\sigma_{\parallel}$ . The iso\_slab model provides  $\chi_{\parallel}$  and  $\sigma_{\parallel}$  that still agree with those obtained  
127 in our two-step experiment, while for the curr\_0 model only  $\sigma_{\parallel}$  looks acceptable. Table 1 reports the

128 optical constants extracted with these different methods. Figures 2a,b, and 3a,b show that the iso\_slab  
129 model and the curr\_0 model are unable to fit the  $\Psi_i$  and  $\Delta_i$ .

130 We also measure the reflectivities  $R_{is} = |r_{is}^2|$  and  $R_{ip} = |r_{ip}^2|$  (figs 2e, 3e). The observed values of  $R_{is}$  and  
131  $R_{ip}$  confirm the good quality of the ellipsometric data because we can properly fit them with the optical  
132 constants extracted from the slab and the curr model. For graphene  $R_{is}$  is one order of magnitude smaller  
133 than for MoS<sub>2</sub>. For  $p$  polarization we observe a pseudo-Brewster angle  $\theta_{pB}$ . The existence and the value of  
134  $\theta_{pB}$  are very important in assessing the vertical anisotropy of single-layer graphene and MoS<sub>2</sub> (table 1).  
135 The iso\_slab model predicts a wrong  $\theta_{pB}$ , the curr\_0 model does not predict it at all.

136 It is possible to discriminate in between the curr model and the slab model thanks to *ab initio* calculations  
137 that predict a positive  $\chi_{\perp}$ <sup>24</sup>. Reference<sup>23</sup> computes only  $\sigma_{\perp}$ , but Kramers-Kronig relations exclude a  
138 negative  $\chi_{\perp}$  in the visible spectrum even in this case. We also performed first-principles calculations  
139 explicitly focused in the visible domain (figs. 3 and 4. Extended data section). By considering the available  
140 theoretical predictions and the experimental data collected here, the surface current model seems the  
141 only one able to fit the data in good agreement with the computed optical constants.

142 The study of a 2D crystal deposited on a substrate or immersed in a host material is by far the most  
143 common situation in laboratory. Still, measuring a free-standing monolayer<sup>30</sup> will be of great interest. If  
144 macroscopically it means a 2D crystal immersed in a medium with  $n = 1$  rather than 1.4233,  
145 microscopically it addresses the question on how much the host material affects the value of  $\chi_{\perp}$ , if by an  
146 experimentally appreciable quantity or less.

147 We have observed the role of  $\vec{P}_{\perp}$  in a single-layer 2D crystal, showing that it affects dramatically the  
148 position of  $\theta_{pB}$ . Our results state that  $\chi_{\perp}$  is a measurable optical constant way different from  $\chi_{\parallel}$  or zero.  
149 These findings will have a deep impact in 2D crystal optics, opening new perspectives for fundamental

150 science and technical developments. Based on present knowledge, we identify a single theoretical  
151 description<sup>26</sup> for a 2D crystal. Contrarily to what sometimes believed<sup>3,4,26</sup>, the slab and the surface current  
152 models are not equivalent even when we take into account  $\vec{P}_\perp$ . Out-of-plane anisotropy in 2D materials  
153 should play a role also in nonlinear optics<sup>13</sup>, surface wave phenomena<sup>14</sup> or magneto-optical Kerr effect<sup>15</sup>  
154 and any other field of 2D crystal optics. In view of the advances in photonics and optoelectronics of 2D  
155 semiconductors<sup>16,17</sup>, we expect a precise characterization of  $\chi_\perp$  and  $\sigma_\perp$  to become of great importance. A  
156 relevant open question is to what extent these quantities can be tuned in hetero-structures for new  
157 functionalities<sup>31</sup>.

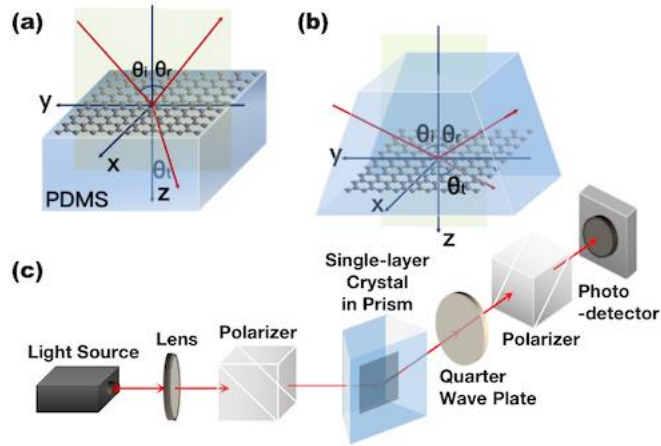
158

Monolayer	Model	$\chi_{\parallel}$ (nm)	$\sigma_{\parallel}$ ( $10^{-5} \Omega^{-1}$ )	$\chi_{\perp}$ (nm)	$\sigma_{\perp}$ ( $10^{-6} \Omega^{-1}$ )	$\theta_{pB}$
Graphene	curr	$1.7 \pm 0.2$	$6.8 \pm 0.3$	$0.6 \pm 0.2$	$3 \pm 3$	$56.5^{\circ}$
	slab	$2.1 \pm 0.2$	$6.8 \pm 0.6$	$-0.9 \pm 0.5$	$9 \pm 9$	$56.3^{\circ}$
	iso_slab	$1.8 \pm 0.2$	$6.8 \pm 0.4$	$1.8 \pm 0.2$	$68 \pm 4$	$65.3^{\circ}$
	curr_0	$1.3 \pm 0.2$	$6.8 \pm 0.4$	0	0	No
MoS <sub>2</sub>	curr	$10.8 \pm 0.5$	$15.0 \pm 0.4$	$1.1 \pm 0.4$	$1 \pm 3$	$66.4^{\circ}$
	slab	$11.2 \pm 0.8$	$14.7 \pm 0.4$	$-2.7 \pm 1.2$	$14 \pm 41$	$67.9^{\circ}$
	iso_slab	$11.4 \pm 0.5$	$15.7 \pm 0.4$	$11.4 \pm 0.5$	$157 \pm 4$	$73.0^{\circ}$
	curr_0	$10.1 \pm 0.5$	$15.7 \pm 0.4$	0	0	No

159

160 Table 1 **Optical constants for monolayer graphene and MoS<sub>2</sub>**. For the curr and the slab models we report  
161 the average of the  $(\chi_{\parallel}, \sigma_{\parallel}, \chi_{\perp}, \sigma_{\perp})$  extracted from the  $(\Psi_s, \Delta_s, \Psi_i, \Delta_i)$ . The error in this case is the standard  
162 deviation of these values. For the iso-slab and the curr\_0 model we report the  $\chi_{\parallel}, \sigma_{\parallel}$  ( $\chi_{\perp}, \sigma_{\perp}$  being trivially  
163 fixed) extracted from the  $(\Psi_s, \Delta_s)$ .  $\theta_{pB}$ : pseudo- Brewster angle expected for the different models.

164



165

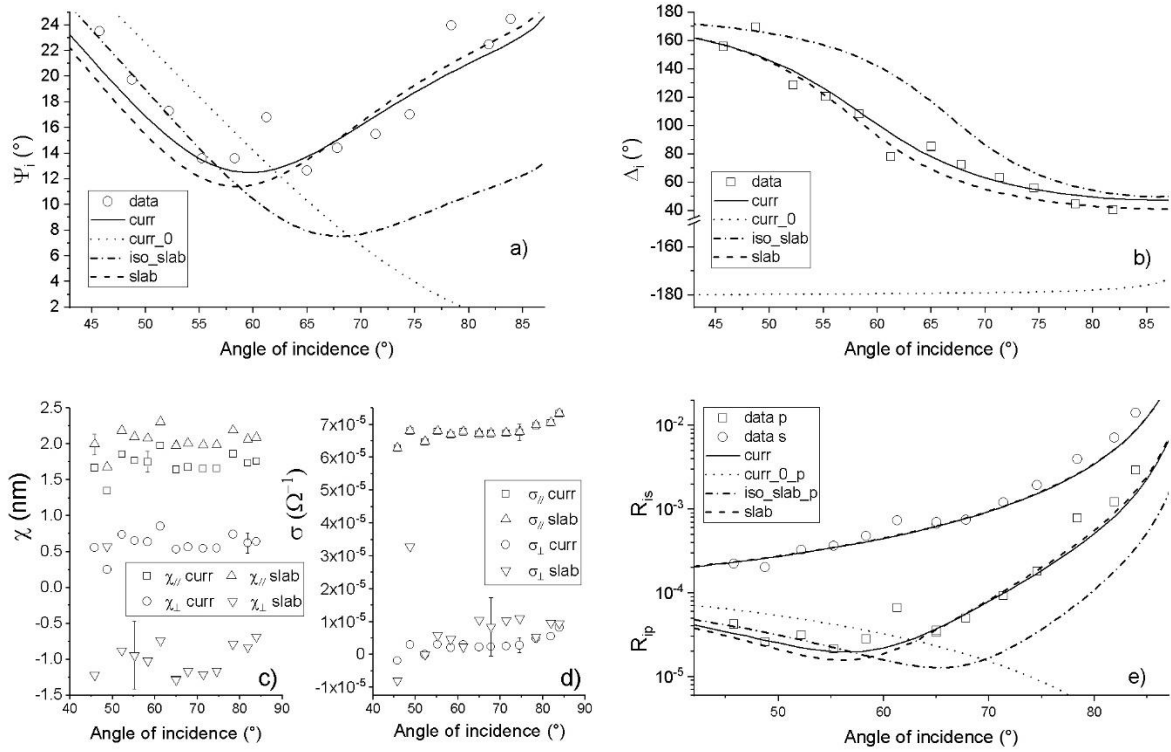
166 **Fig. 1 Experimental set up. a**, scheme of the standard spectroscopic ellipsometry on a single-layer 2D

167 crystal deposited on a PDMS substrate. **b**, scheme of the manual ellipsometric measurement on the same

168 crystal completely immersed in a PDMS prism. **c**, set up of the manual ellipsometer, at the wavelength of

169 633 nm.

170



171

172

173 **Fig. 2 Experimental results for monolayer graphene immersed in PDMS.** Dots: experimental data, Lines:

174 theoretical fits for the four models considered in this paper. **a, b**, ellipsometric parameters  $\Psi_i$  and  $\Delta_i$ .

175 Neither the iso\_slab model nor the curr\_0 model fit the data, using as optical constants those extracted

176 from the  $\Psi_s$  and  $\Delta_s$ . **c, d**, optical constants determined with slab and the curr model. They predict similar

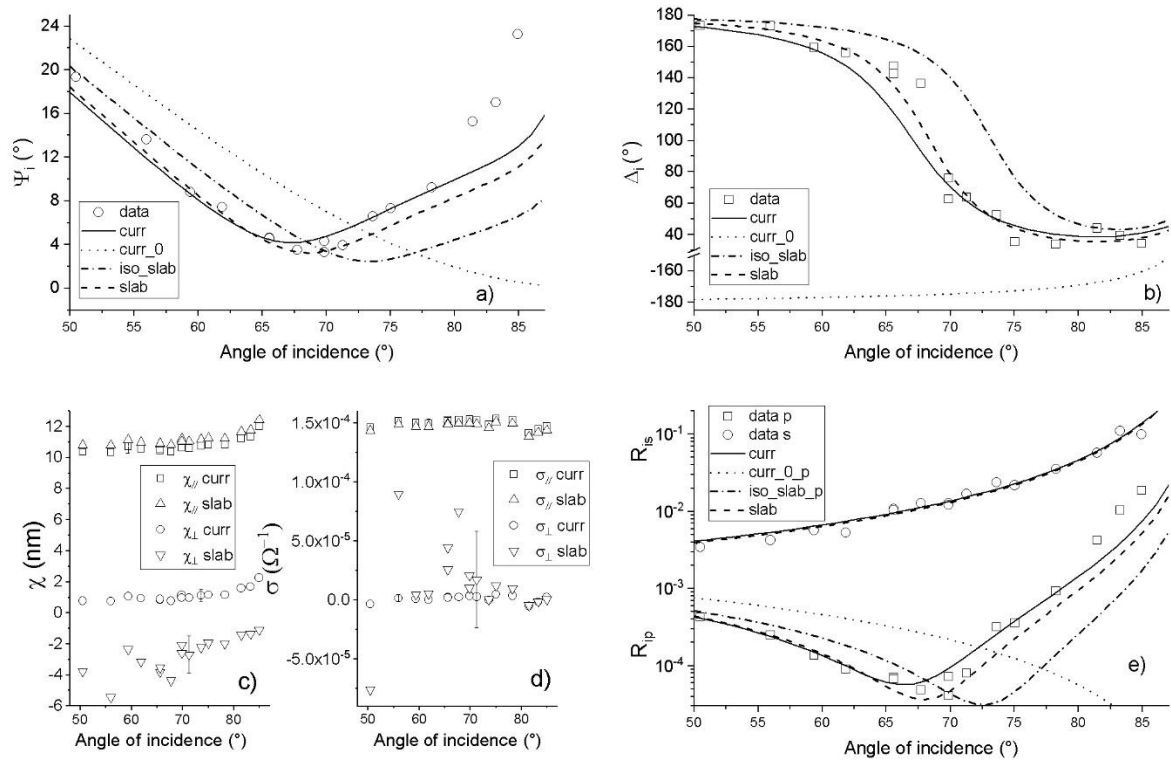
177  $\chi_{||}$  and  $\sigma_{||}$ , but negative and positive  $\chi_{\perp}$  respectively, and  $\sigma_{\perp}$  compatible with  $0 \Omega^{-1}$ . **e**, Reflectivities for  $s$

178 and  $p$  polarized light. Experimental data show a pseudo Brewster angle for  $R_{ip}$ . The iso\_slab model fails to

179 predict its position by almost  $10^\circ$ . The curr\_0 model does not predict it at all. All models fit  $R_{is}$  reasonably

180 well (for clarity we show only the curr model and the slab model).

181



182

183

184 **Fig. 3 Experimental results for monolayer MoS<sub>2</sub> immersed in PDMS.** Dots: experimental data, Lines:

185 theoretical fits for the four models considered in this paper. **a, b**, ellipsometric parameters  $\Psi_i$  and  $\Delta_i$ .

186 Neither the iso\_slab model nor the curr\_0 model fit the data, using as optical constants those extracted

187 from the  $\Psi_s$  and  $\Delta_s$ . **c, d**, optical constants determined with slab and the curr model. They predict similar

188  $\chi_{||}$  and  $\sigma_{||}$ , but negative and positive  $\chi_{\perp}$  respectively, and  $\sigma_{\perp}$  compatible with  $0 \Omega^{-1}$ . **e**, reflectivities for  $s$

189 and  $p$  polarized light. Experimental data show a pseudo Brewster angle for  $R_{ip}$ . The iso\_slab model fails to

190 predict its position by almost  $7^\circ$ . The curr\_0 model does not predict it at all. All models fit  $R_{is}$  reasonably

191 well (for clarity we show only the curr model and the slab model).

192

193 1 Nelson, F. J. *et al.* Optical properties of large-area polycrystalline chemical vapor deposited  
194 graphene by spectroscopic ellipsometry. *Appl. Phys. Lett.* **97**, 253110 (2010).

195 2 Merano, M. Fresnel coefficients of a two-dimensional atomic crystal. *Phys. Rev. A* **93**, 013832  
196 (2016).

197 3 Majérus, B., Dremetsika, E., Lobet, M., Henrard, L. & Kockaert, P. Electrodynamics of two-  
198 dimensional materials: Role of anisotropy. *Phys. Rev. B* **98**, 125419 (2018).

199 4 Li, Y. & Heinz, T. F. Two-dimensional models for the optical response of thin films. *2D Mater.* **5**,  
200 025021 (2018).

201 5 Chang, Y.-C., Liu, C.-H., Liu, C.-H., Zhong, Z. & Norris, T. B. Extracting the complex optical  
202 conductivity of mono- and bilayer graphene by ellipsometry. *Appl. Phys. Lett.* **104**, 261909 (2014).

203 6 Blake, P. *et al.* Making graphene visible. *Appl. Phys. Lett.* **91**, 063124 (2007).

204 7 Bruna, M. & Borini, S. Optical constants of graphene layers in the visible range. *Appl. Phys. Lett.*  
205 **94**, 031901 (2009).

206 8 Li, Y. *et al.* Measurement of the optical dielectric function of monolayer transition-metal  
207 dichalcogenides: MoS<sub>2</sub>, MoSe<sub>2</sub>, WS<sub>2</sub>, and WSe<sub>2</sub>. *Phys. Rev. B* **90**, 125706 (2014).

208 9 Benameur, M. M. *et al.* Visibility of dichalcogenide nanolayers. *Nanotechnology* **22**, 125706  
209 (2011).

210 10 Hanson, G., W. Dyadic Green's functions and guided surface waves for a surface conductivity  
211 model of graphene. *J. Appl. Phys.* **103**, 064302 (2008).

212 11 Falkovsky, L. A. & Pershoguba, S. S. Optical far-infrared properties of a graphene monolayer and  
213 multilayer. *Phys. Rev. B* **76**, 153410 (2007).

214 12 Zhan, T., Shi, X., Dai, Y., Liu, X. & Zi, J. Transfer matrix method for optics in graphene layers. *J. Phys.*  
215 *Condens. Matter* **25**, 215301 (2013).

216 13 Kumar, N. *et al.* Second harmonic microscopy of monolayer MoS<sub>2</sub>. *Phys. Rev. B* **87**, 161403 (2013).

217 14 Fei, Z. *et al.* Gate-tuning of graphene plasmons revealed by infrared nano-imaging. *Nature* **487**,  
218 82-85 (2012).

219 15 Huang, B. *et al.* Layer-dependent ferromagnetism in a van der Waals crystal down to the  
220 monolayer limit. *Nature* **546**, 270-273 (2017).

221 16 Mak, K. F. & Shan, J. Photonics and optoelectronics of 2D semiconductor transition metal  
222 dichalcogenides. *Nat. Photonics* **10**, 216-226 (2016).

223 17 Mak, K. F., Lee, C., Hone, J., Shan, J. & Heinz, T. F. Atomically thin MoS<sub>2</sub>: a new direct-gap  
224 semiconductor. *Phys. Rev. Lett.* **105**, 136805 (2010).

225 18 Kravets, V. G. *et al.* Spectroscopic ellipsometry of graphene and an exciton-shifted van Hove peak  
226 in absorption. *Phys. Rev. B* **81**, 155413 (2010).

227 19 Funke, S., Miller, B., Parzinger, E., Thiesen, P. & Wurstbauer, U. Imaging spectroscopic  
228 ellipsometry of MoS<sub>2</sub>. *J. Phys. Condens. Matter* **28**, 385301 (2016).

229 20 Chu, Y. & Zhang, Z. Birefringent and complex dielectric functions of monolayer WSe<sub>2</sub> derived by  
230 spectroscopic ellipsometer. *J. Phys. Chem. C* **124**, 12665-12671 (2020).

231 21 Gaurav, J. *et al.* Measurement of the surface susceptibility and the surface conductivity of  
232 atomically thin MoS<sub>2</sub> by spectroscopic ellipsometry. *Opt. Lett.* **43**, 703-706 (2018).

233 22 Li, W. *et al.* Broadband optical properties of large-area monolayer CVD molybdenum disulfide.  
234 *Phys. Rev. B* **90**, 195434 (2014).

235 23 Trevisanutto, P. E., Holzmann, M., Coté, M. & Olevano, V. *Ab initio* high-energy excitonic effects  
236 in graphite and graphene. *Phys. Rev. B* **81**, 121405 (2010).

237 24 Guilhon, I. *et al.* Out-of-plane excitons in two-dimensional crystals. *Phys. Rev. B* **99**, 161201 (2019).

238 25 Azzam, R. M. A. & Bashara, N. M. *Ellipsometry and polarized light*. 356-357 (NORTH-HOLLAND  
239 PUBLISHING COMPANY-AMSTERDAM, 1977).

240 26 Senior, T. B. A. & Volakis, J. L. Sheet simulation of a thin dielectric layer. *Radio Sci.* **22**, 1261-1272  
241 (1987).  
242 27 Idemen, M. Universal boundary relations of the electromagnetic field. *J. Phys. Soc. Japan* **59**, 71-  
243 80 (1990).  
244 28 Kuester, E. F., Mohamed, M. A., Piket-May, M. & Holloway, C. L. Averaged transition conditions  
245 for electromagnetic fields at a metafilm. *IEEE Trans. Antennas Propag.* **51**, 2641-2651 (2003).  
246 29 Jackson, J. D. *Classical Electrodynamics, 3rd ed.*, 413-414 (Wiley, New York, 1998).  
247 30 Nair, R. R. *et al.* Fine structure constant defines visual transparency of graphene. *Science* **320**,  
248 1308 (2008).  
249 31 Geim, A. K. & Grigorieva, I. V. Van der Waals heterostructures. *Nature* **499**, 419-425 (2013).  
250  
251

252 **Methods**

253 1. Fresnel coefficients for the curr model ( $p$ -polarization)

254 a. Insulator single-layer 2D crystal immersed in a dielectric medium of refractive index  $n$ .

255 The electromagnetic fields satisfy:  $\frac{\eta}{n} \vec{H} = \hat{s} \wedge \vec{E}$ ,  $\hat{s}$  being the unit vector along the propagation direction.

256 We compute the reflected field due to  $\vec{J}_{\parallel}$  by solving the boundary equations (1). In this case, the electric

257 field parallel to the crystal plane is continuous across the crystal itself giving:  $\vec{P}_{\parallel} = \varepsilon_0 \chi_{\parallel} \vec{E}_{\parallel}$  (5). Choosing<sup>2</sup>

258  $\vec{H}$  along  $-\hat{i}$ , equations (1) plus (5) run:

259 
$$H_i + H_{r1} - H_{t1} = \frac{i k}{\eta \varepsilon_0} P_{\parallel}$$

260 
$$H_i - H_{r1} = H_{t1}$$

261 
$$H_{t1} = \frac{n P_{\parallel}}{\eta \varepsilon_0 \chi_{\parallel} \cos \theta}$$

262 Where the subscript  $i, r, t$  denote the incident, reflected and transmitted fields. We compute the reflected

263 field due to  $\vec{J}_{\perp}$  by solving the boundary equations (2). In this case, the electric field orthogonal to the

264 crystal plane is continuous across the crystal itself giving:  $\vec{P}_{\perp} = \varepsilon_0 \chi_{\perp} \vec{E}_{\perp}$  (6). Choosing  $\vec{H}$  along  $-\hat{i}$ ,

265 equations (2) plus (6) run:

266 
$$H_i + H_{r2} = H_{t2}$$

267 
$$H_i - H_{r2} - H_{t2} = \frac{i k n^2 P_{\perp} \tan \theta}{\eta \varepsilon_0}$$

268 
$$H_{t2} = \frac{n P_{\perp}}{\eta \varepsilon_0 \chi_{\parallel} \sin \theta}$$

269 In accordance to the superposition principle, the total reflected field is:  $H_r = H_{r1} + H_{r2}$ , the total  
 270 transmitted field is:  $H_t = H_{t1} + H_{t2} - H_i = H_i - H_{r1} + H_{r2}$ . The reflection and the transmission  
 271 coefficients are respectively:  $r_{ip} = \frac{H_r}{H_i}$ ;  $t_{ip} = \frac{H_t}{H_i}$ . We verify that:  $R_{ip} + T_{ip} = 1$ , where  $T_{ip} = |t_{ip}^2|$ .

272 b. Insulator single-layer 2D crystal at the vacuum – dielectric medium interface.

273 The electromagnetic fields in vacuum satisfy:  $\eta \vec{H} = \hat{s} \wedge \vec{E}$ . For  $\vec{J}_{\parallel}$  equations (1) plus (5) run:

$$274 \quad H_i + H_{r1} - H_{t1} = \frac{i k}{\eta \epsilon_0} P_{\parallel}$$

$$275 \quad (H_i - H_{r1}) \cos \theta = \frac{H_{t1} \cos \theta_t}{n}$$

$$276 \quad H_{t1} = \frac{n P_{\parallel}}{\eta \epsilon_0 \chi_{\parallel} \cos \theta_t}$$

277 For  $\vec{J}_{\perp}$  equations (2) plus (6) run:

$$278 \quad H_i + H_{r2} = H_{t2}$$

$$279 \quad (H_i - H_{r2}) \cos \theta - \frac{H_{t2} \cos \theta_t}{n} = \frac{i k P_{\perp} \sin \theta}{\eta \epsilon_0}$$

$$280 \quad H_{t2} = \frac{n^2 P_{\perp}}{\eta \epsilon_0 \chi_{\parallel} \sin \theta}$$

281 In accordance to the superposition principle, the total reflected field is:  $H_r = H_{r1} + H_{r2} - H_{rn}$ , the total  
 282 transmitted field is:  $H_t = H_{t1} + H_{t2} - H_{tn}$ , where  $H_{rn}$  and  $H_{tn}$  are the fields reflected and transmitted  
 283 without the 2D crystal deposited at the interface. The Fresnel coefficients are defined as above, and from  
 284 energy flux considerations:  $R_{ip} + \frac{n \cos \theta_t}{\cos \theta} T_{ip} = 1$ . Thanks to the application of the superposition principle,  
 285 our connection of  $\vec{P}_{\parallel}$  and  $\vec{P}_{\perp}$  with the macroscopic field is straightforward. This principle is not usually

286 applied in the literature of metamaterials<sup>28</sup> forcing to definitions different from (5) and (6). Unfortunately,  
287 this last approach does not seem to verify energy flux conservation that we expect valid for insulators.

288 For conducting 2D crystals we have to modify the definition of  $\vec{J}_{\parallel}$  in (1):  $\vec{J}_{\parallel} = \frac{\partial \vec{P}_{\parallel}}{\partial t} + \vec{J}_{\sigma_{\parallel}}$ , where:  $\vec{J}_{\sigma_{\parallel}} =$   
289  $\sigma_{\parallel} \vec{E}_{\parallel}$  (7) and the definition of  $\vec{J}_{\perp}$  in (2)<sup>27</sup>:  $\vec{J}_{\perp} = -\frac{1}{\epsilon_0} \hat{k} \wedge grad \left( P_{\perp} + \frac{J_{\sigma_{\perp}}}{i\omega} \right)$  where:  $\vec{J}_{\sigma_{\perp}} = \sigma_{\perp} \vec{E}_{\perp}$  (8). We  
290 then compute the reflected and the transmitted fields due to  $\vec{J}_{\parallel}$  by solving equations (1), (5) and (7) and  
291 those due to  $\vec{J}_{\perp}$  by solving equations (2), (6) and (8).

## 292 2. Sample preparation

### 293 a. Monolayer Graphene growth and transfer.

294 We have prepared one large-area (up to millimeters), polycrystalline, continuous, single-layer graphene  
295 with chemical vapor deposition (CVD). Monolayer graphene grows on commercial Cu foils (50  $\mu\text{m}$  thick,  
296 Kunshan luzhifa Electronic Technology Co., Ltd) via a low-pressure CVD system. Cu foil is annealed at  
297 1020 °C under a 500 sccm flow of Ar with a 0.1 sccm flow of O<sub>2</sub> (0.1% of diluted O<sub>2</sub> in Ar) for 30 min. Then,  
298 graphene grows under 500 sccm flow of H<sub>2</sub> and a step increased flow rate of CH<sub>4</sub> (0.5 sccm for 20 min, 0.8  
299 sccm for 20 min, and then 1.2 sccm for 40 min)<sup>32</sup>. For the graphene transfer, poly(methyl-methacrylate)  
300 (PMMA) is spin-coated on as-grown graphene on Cu at 2000 rpm and baked at 170 °C for 3 min. The Cu  
301 foil is then etched away by NaS<sub>2</sub>O<sub>8</sub> (1 mol/L) after the graphene on the other side of Cu (graphene was  
302 grown on both sides of Cu foils) is removed by air plasma (10 sccm and power of 100 W). Subsequently,  
303 the freestanding PMMA/graphene stack floating on NaS<sub>2</sub>O<sub>8</sub> solution is washed with deionized water for 4  
304 times, and salvaged by the PDMS, forming the PMMA/graphene/PDMS structure. After the as-formed  
305 PMMA/graphene/PDMS is dried, the PMMA is removed by immersion in acetone at 80 °C for 10 min and  
306 it forms the graphene /PDMS structure.

### 307 b. Monolayer MoS<sub>2</sub> growth and transfer.

308 We have prepared one large-area (up to millimeters), polycrystalline, continuous, single-layer MoS<sub>2</sub> with  
309 chemical vapor deposition (CVD). Monolayer MoS<sub>2</sub> grows on soda-lime glass using a three-zone tube  
310 furnace under low-pressure atmosphere. A piece of Mo foil (Alfa Aesar, 9.95%; 0.025mm thick) was  
311 folded as a “bridge” and placed on top of the glass substrate with a gap of 10 mm. S powder (Alfa Aesar,  
312 purity 99.5%) was located at the upstream of the furnace. Before heating, the system was purged  
313 with Ar (80 sccm) for 10 min to get out of the air. Then, Ar (50 sccm) and O<sub>2</sub> (6 sccm) mixed gas flows were  
314 introduced into the system to create a stable growth atmosphere. The temperature of the  
315 S powder and the glass substrate were set at 100 °C and 720 °C, respectively. The growth time was set at  
316 1–3 min. After growth, the furnace was naturally cooled to room temperature. The as-synthesized MoS<sub>2</sub>  
317 monolayer/soda-lime samples were firstly spin-coated with PMMA at 1000 rpm for 1 min, followed by  
318 baking at 80 °C for 20 min. The PMMA-supported samples were then inclined into the pure water, and the  
319 PMMA/MoS<sub>2</sub> complex was naturally peeled off under the surface tension effect. The PMMA/MoS<sub>2</sub> film  
320 was collected by PDMS. Finally, the PMMA film was removed via acetone.

321 c. PDMS substrate preparation and immersion of the 2D crystal in PDMS.

322 The PDMS (Sylgard 184, by Dow Corning) substrate is prepared by mixing the base elastomer and the  
323 curing agent in ratio 10:1, and by 72 hours room temperature (RT) polymerization. Then, after the  
324 deposition of the monolayer 2D crystal (see above), new pre-polymerized PDMS is poured on the  
325 structure, using a 3D printed prism shape structure (ABS filament) as mold. We again wait for RT  
326 polymerization. Since the 3D printed structure presents a high roughness that would compromise the  
327 optical measurements, glass slides are glued on them. In this way, we obtain a PDMS prism with optical  
328 quality lateral windows. To prevent the PDMS bonding to the glass slides during the polymerization  
329 process, a fluorinated antiadhesive coating (Trichloro(1H,1H,2H,2H-perfluorooctyl)silane, by Sigma-  
330 Aldrich) is applied.

331 3. Measurement and determination of the optical constants

332 a. Spectroscopic ellipsometry of a 2D Crystal deposited on a PDMS substrate.

333 Spectroscopic ellipsometric measurements are performed using a VASE ellipsometer (J. A. Wollam) in  
334 ambient conditions at room temperature. We follow the same procedure described in<sup>21</sup>. The first step of  
335 our analysis is the characterization of the substrate. The ellipsometric  $\Psi$  parameter of the substrate alone  
336 is perfectly fitted by assuming a refractive index  $n$  given by the Sellmeier expression<sup>33</sup> minus a constant  
337 value of 0.005. At a wavelength of 633 nm we have  $n = 1.4233$ . For graphene, the use of this measured  
338 value instead of the one reported in the literature<sup>33</sup> is responsible for a difference of 0.06 nm,  $1 \cdot 10^{-6} \Omega^{-1}$ ,  
339 0.06 nm and  $9 \cdot 10^{-6} \Omega^{-1}$  respectively for  $\chi_{\perp}$ ,  $\sigma_{\perp}$ ,  $\chi_{\parallel}$  and  $\sigma_{\parallel}$ . Only the discrepancy for  $\sigma_{\parallel}$  is bigger than the  
340 error in the measurements (Table 1). Although small, this last difference shows the importance of a careful  
341 substrate characterization when dealing with monolayers. For MoS<sub>2</sub> these discrepancies are even smaller  
342 than for graphene and equal respectively to 0.02 nm,  $7 \cdot 10^{-7} \Omega^{-1}$ , 0.03 nm and  $9 \cdot 10^{-6} \Omega^{-1}$ .

343 Figures 1 and 2 (extended data section) show the ellipsometric parameter  $\Psi_s$  and  $\Delta_s$  of single-layer  
344 graphene and MoS<sub>2</sub> deposited on a PDMS substrate. Starting from these data, reference<sup>21</sup> describes how  
345 we extract  $\chi_{\parallel}$  and  $\sigma_{\parallel}$  for the iso\_slab model and the curr\_0 model.

346 b. Manual ellipsometer

347 The light source is a HeNe laser at a wavelength of 633 nm. A lens (focal length 40 cm) focuses the Gaussian  
348 beam to a  $1/e^2$  intensity diameter of 120  $\mu\text{m}$  allowing measurements at grazing incidence. We set the first  
349 polarizer at an azimuthal angle of 45°. The light intensity after the first polarizer is typically 4 mW. A  
350 quarter wave plate (QWP) and a second polarizer (the analyzer) perform ellipsometric measurements. We  
351 fully characterize the vibrational ellipse for the electric vector of the light reflected from the sample<sup>34</sup>.  
352 Without the QWP installed, we measure the  $s$  and  $p$  components of the reflected light. Then we identify  
353 the azimuthal angles of the minor and the major axes of the ellipse. Finally we place the QWP with the

354 fast axis along the minor axis. After this, the azimuthal angle of the analyzer, corresponding to a minimum  
355 power on the photodetector, fixes the sense in which the endpoint of the electric vector describes the  
356 ellipse (the sign of  $\Delta_i$ ). The power meter used in our measurements has a resolution of 1 nW. Only the 2D  
357 crystal introduces a phase difference ( $\Delta_i$ ) in between the  $s$  and  $p$  components of the incident linearly  
358 polarized light. Transmission through the two prism sides only introduces a different power reduction in  
359  $s$  and  $p$ , important for the correct evaluation of  $\Psi_i$ ,  $R_{is}$  and  $R_{ip}$ . The QWP is antireflection coated at 633  
360 nm while the analyzer introduces an identical power reduction in  $s$  and  $p$  (important for a correct  
361 evaluation of  $R_{is}$  and  $R_{ip}$ ).

362 We are unable to estimate  $\sigma_{\perp}$  because it is much smaller (fig. 6 Extended data section) than our  
363 experimental error. We are limited by the quality of the reflected beam and by some scattering. The poor  
364 quality of the reflected beam is a consequence of the macroscopic quality of our 2D crystals. Even if we  
365 are dealing with some of the best samples available in the world, any small defect affects the reflection  
366 of a highly coherent laser source. A few amount of unwanted scattering comes from the back surface of  
367 the prism that is far from perfect because of handling or, for some angles of incidence, from the prism  
368 corners.

#### 369 4. First-principles calculations

370 Layer susceptibilities have been evaluated using first-principles many-body perturbation theory  
371 calculations of periodic dielectric layers. First, density functional theory (DFT) orbitals were obtained with  
372 the so-called PBE exchange and correlation functional<sup>35</sup> at the theoretical lattice constant using the  
373 Quantum-Espresso DFT software package<sup>36</sup>. Then, the screened Coulomb interaction  $W$ <sup>37</sup> was found using  
374 the  $G_0W_0$  approach (GWL program<sup>38</sup>). The Brillouin zones were sampled at the sole  $\Gamma$  point albeit adopting  
375 supercells comprising 8 atoms for graphene and 12 atoms for MoS<sub>2</sub>. An optimal polarizability basis of 800  
376 vectors was applied for developing the polarizability operators. Finally, the in-plane  $\varepsilon_{//}$  and out-of-plane

377  $\epsilon_{\perp}$  components of the complex dielectric tensors relative to the periodic thin dielectric layers were  
378 calculated including electron-hole interactions using the Bethe-Salpeter equation scheme<sup>39,40</sup> (simple.x  
379 code<sup>41</sup>).

380 For graphene, we used a 12 x 12 x 12 regular mesh of k-points for sampling the Brillouin zone (relative to  
381 the super-cell) which was shifted in order not to contain the  $\Gamma$  point and we included 12 occupied and 48  
382 unoccupied orbitals. A stretching factor of 1.67 was applied to the DFT valence and conduction bands in  
383 order to match GW energies in the proximity of the band closure at the  $K$ -point. These GW values were  
384 obtained extrapolating, to the bulk limit, results for models of 12 and 32 atoms.

385 For MoS<sub>2</sub>, we used a 6 x 6 x 6 regular mesh of k-points for sampling the Brillouin zone (relative to the  
386 super-cell) together with a fully relativistic treatment of the spin-orbit coupling. We included 56 occupied  
387 and 96 unoccupied orbitals. A scissor factor of 1.30 eV was applied to the DFT band structure in order that  
388 the DFT gap matches the bulk limit of the GW one. The latter was evaluated at the scalar relativistic level.  
389 Moreover, for MoS<sub>2</sub> we added a constant term of 2.13 to  $\epsilon_{\parallel}$  and one of 1.33 to  $\epsilon_{\perp}$  in order to account for  
390 the upper unoccupied orbitals which were not included in the BSE calculation. These factors were chosen  
391 in order to match the corresponding components of the dielectric tensor calculated from density  
392 functional perturbation theory.

393 It is worth noting that the calculated BSE susceptibilities exhibit only a mild dependence on the strategy  
394 chosen for updating the DFT bands in order to account for GW effects. In particular, the out-of-plane  
395 responses are particularly insensitive as it is shown, for MoS<sub>2</sub> in Figs. 5 and 6 of the extended data section  
396 where we report results obtained using scissor factors of 1.0, 1.3 eV and a scissor factor of 1.0  
397 accompanied by a stretching one of 1.2 for both manifolds as in ref.<sup>42</sup>.

398 The in-plane  $\chi_{C\parallel}$  and out-of-plane  $\chi_{C\perp}$  complex susceptibilities are rigorously defined as the ratio between  
399 the induced surface dipole densities with respect to the transmitted electric field. In the case of  $\chi_{C\parallel}$  the

400 transmitted field is parallel to the 2D layer and is conserved along the simulation cell. It is worth noting<sup>43</sup>  
 401 that in first-principles simulations with periodic boundary conditions (PBC) the directly accessible quantity  
 402 is the response with respect to the total or internal (electric) field. This is due to incommensurate  
 403 extension of the field with respect to the length period of the PBC. This makes it possible to obtain  $\chi_{C\parallel}$   
 404 from  $\varepsilon_{\parallel}$ :

$$405 \quad \chi_{C\parallel} = L (\varepsilon_{\parallel} - 1) \quad (9)$$

406 where  $L$  is the periodic length of the simulation cell in the direction perpendicular to the 2D layer. This  
 407 length is big from a microscopic point of view in order to null the interaction between the atomic layers  
 408 but small from a macroscopic point of view (for instance it is much smaller than the wavelength of the  
 409 incident light).

410 For  $\chi_{C\perp}$  the transmitted electric field  $E_{t\perp}$ , which is now perpendicular to the 2D layer, can be found<sup>43</sup> from  
 411  $\varepsilon_{\perp}$ :

$$412 \quad E_{t\perp} = \frac{E_{cell}}{\varepsilon_{\perp}} \quad (10)$$

413 where  $E_{cell}$  is the perpendicular long-range electric field accounted for in the calculation of  $\varepsilon_{\perp}$ . Hence, the  
 414 out-of-plane complex susceptibility is given by:

$$415 \quad \chi_{C\perp} = \frac{L(\varepsilon_{\perp}-1)}{\varepsilon_{\perp}} \quad (11)$$

416 Equations. 1 and 3 have been reported previously<sup>24,26</sup>. Reference<sup>24</sup> derive them to model a dielectric layer  
 417 as an infinitesimally thin sheet. Reference<sup>26</sup> derives them from the effects of local fields to the dielectric  
 418 responses.

419 For evaluating  $\varepsilon_{\parallel}$  and  $\varepsilon_{\perp}$ , we applied first a Lorentzian broadening of 0.1 eV and then a Gaussian one of  
 420 0.2 eV<sup>23</sup>. The surface susceptibilities measured in this paper are the real part of  $\chi_{C\parallel}$  and  $\chi_{C\perp}$ , the surface  
 421 conductivities are proportional to the imaginary part of  $\chi_{C\parallel}$  and  $\chi_{C\perp}$ <sup>8,21</sup>. Figures 3 and 4 (extended data

422 section) report the computed out-of-plane optical constants in the visible spectrum. The in-plane optical  
423 constants are similar to those already reported in refs.<sup>23,24,42</sup>.

- 424 32 Sun, L. *et al.* Visualizing fast growth of large single-crystalline graphene by tunable isotopic carbon  
425 source. *Nano Res.* **10**, 355-363 (2016).
- 426 33 Schneider, F., Draheim, J., Kamberger, R. & Wallrabe, U. Process and material properties of  
427 polydimethylsiloxane (PDMS) for optical MEMS. *Sensor Actuat. A: Phys.* **151**, 95-99 (2009).
- 428 34 Born, M. & Wolf, E. *Principles of optics, 5th ed.*, Chap. 1 (Pergamon Press, London, 1975).
- 429 35 Perdew, J. P., Burke, K. & Ernzerhof, M. Generalized gradient approximation made simple. *Phys.*  
430 *Rev. Lett.* **77**, 3865-3868 (1996).
- 431 36 Giannozzi, P. *et al.* Advanced capabilities for materials modelling with Quantum ESPRESSO. *J. Phys.*  
432 *Condens. Matter* **29**, 465901 (2017).
- 433 37 Hybertsen, M. S. & Louie, S. G. Electron correlation in semiconductors and insulators: Band gaps  
434 and quasiparticle energies. *Phys. Rev. B* **34**, 5390-5413 (1986).
- 435 38 Umari, P., Stenuit, G. & Baroni, S. GW quasi-particle spectra from occupied states only. *Phys. Rev.*  
436 *B* **81**, 115104 (2009).
- 437 39 Albrecht, S., Reining, L., Del Sole, R. & Onida, G. Ab initio calculation of excitonic effects in the  
438 optical spectra of semiconductors. *Phys. Rev. Lett.* **80**, 4510-4513 (1998).
- 439 40 Rohlfing, M. & Louie, S. G. Electron-hole excitations in semiconductors and insulators. *Phys. Rev.*  
440 *Lett.* **81**, 2312-2315 (1998).
- 441 41 Prandini, G., Galante, M., Marzari, N. & Umari, P. SIMPLE code: Optical properties with optimal  
442 basis functions. *Comput. Phys. Commun.* **240**, 106-119 (2019).
- 443 42 Elliott, J. D. *et al.* Surface susceptibility and conductivity of MoS<sub>2</sub> and WSe<sub>2</sub> monolayers: A first-  
444 principles and ellipsometry characterization. *Phys. Rev. B* **101**, 045414 (2020).
- 445 43 Stengel, M., Spaldin, N. A. & Vanderbilt, D. Electric displacement as the fundamental variable in  
446 electronic-structure calculations. *Nat. Phys.* **5**, 304-308 (2009).

447

448

449

450 **Acknowledgements** Z.X and M.Me acknowledge financial support from Dipartimento di Fisica e  
451 Astronomia G. Galilei, Università Degli Studi di Padova, funding BIRD170839/17. F.D acknowledges STARS  
452 grant from Università Degli Studi di Padova.

453

454

455 **Author contributions** D.F. preparation of PDMS substrate and prism. L.S. Y.W. and Z.L. growth and transfer  
456 of graphene, P.Y and Y.Z growth and transfer of MoS<sub>2</sub>, Z.X., A.Z., N.G., A.M. and M.Me optical

457 measurements and data analysis, L.D.A. and M.Me. analytical theory, J.D.E. and P.U. ab-initio calculations  
458 for MoS<sub>2</sub>, M.Ma. and P.U. ab-initio calculations for graphene, M.Me conceived the idea for the paper and  
459 drafted this manuscript. L.S., P.Y., M.Me, D.F. and P.U. wrote the section Methods. The manuscript was  
460 then read, improved and finally acknowledged by the other authors.

461

462 **Competing interests** The authors declare no competing interests.

463

464 **Additional information**

465 **Correspondence and requests for materials** should be addressed to M.Me.

466

467

468

469

470

471

472

473

474

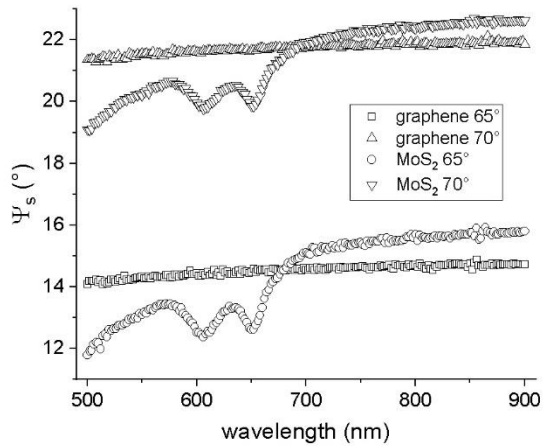
475

476

477

478

479 Extended data section

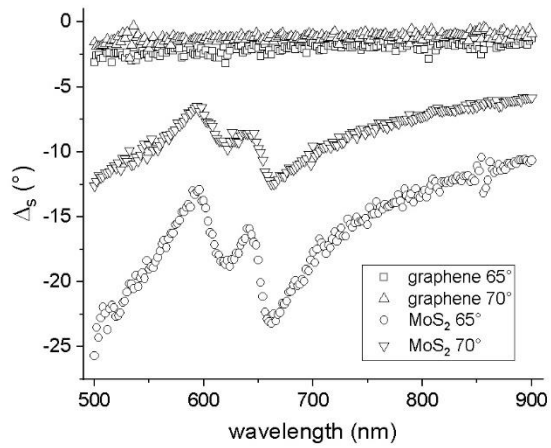


480

481 **Extended data Fig. 1 Ellipsometric parameter  $\Psi_s$  of single layer graphene and MoS<sub>2</sub> deposited on a PDMS**

482 **substrate.** Measurements are taken at angles of incidence  $\theta_s = 65^\circ$  and  $\theta_s = 70^\circ$ .

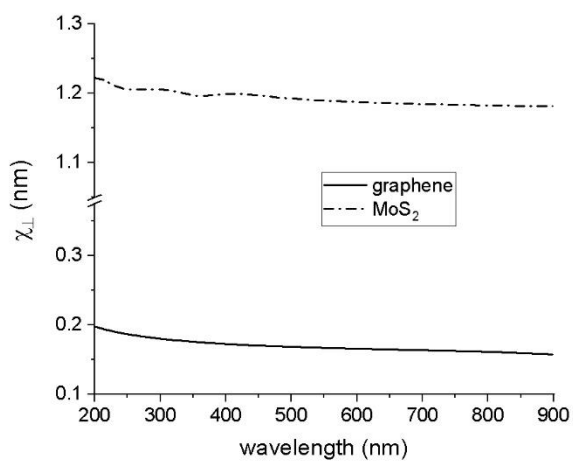
483



484

485 **Extended data Fig. 2 Ellipsometric parameter  $\Delta_s$  of single layer graphene and MoS<sub>2</sub> deposited on a PDMS**

486 **substrate.** Measurements are taken at angles of incidence  $\theta_s = 65^\circ$  and  $\theta_s = 70^\circ$ .

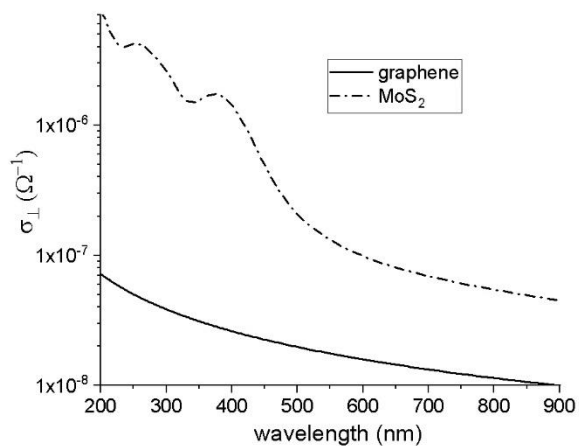


487

488 **Extended data Fig. 3** *Ab initio* calculations for  $\chi_{\perp}$ . The  $\chi_{\perp}$  for a monolayer MoS<sub>2</sub> is bigger than the  $\chi_{\perp}$  of

489 monolayer graphene. The experimental data confirm these expectations.

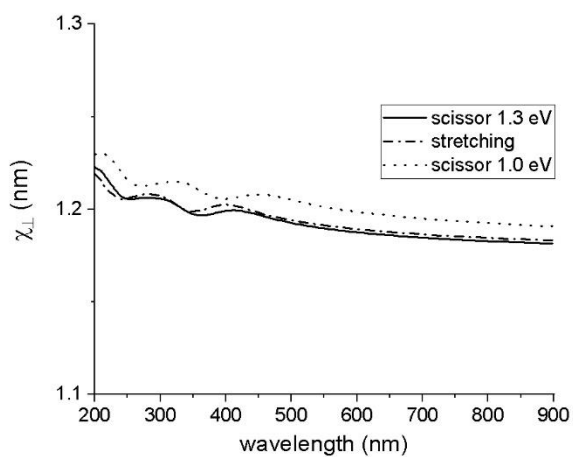
490



491

492 **Extended data Fig. 4** *Ab initio* calculations for  $\sigma_{\perp}$ . The  $\sigma_{\perp}$  for a monolayer MoS<sub>2</sub> is bigger than the  $\sigma_{\perp}$  of  
 493 monolayer graphene. Both quantities are below the experimental sensitivity.

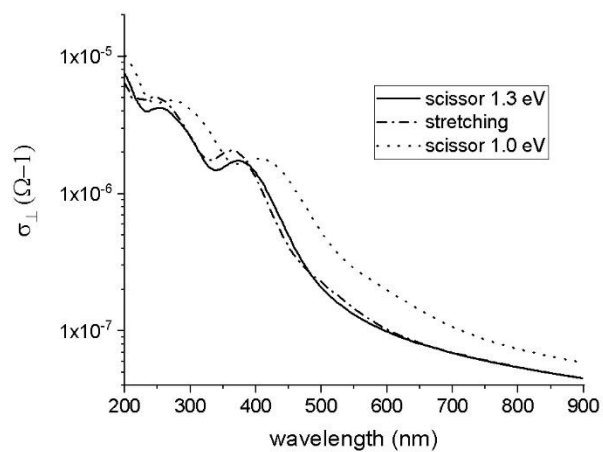
494



495

496 **Extended data Fig. 5 *Ab initio* calculations: GW effects on  $\chi_L$ .** A scissor of 1.3 eV is the choice of the  
 497 previous graphs. A scissor factor of 1.0 eV and a scissor factor of 1.0 eV followed by a stretching of 1.2  
 498 mildly change the final value.

499



500

501 **Extended data Fig. 6 *Ab initio* calculations: GW effects on  $\sigma_{\perp}$ .** A scissor of 1.3 eV is the choice of the  
 502 previous graphs. A scissor factor of 1.0 eV and a scissor factor of 1.0 eV followed by a stretching of 1.2  
 503 mildly change the final value.

504

# Figures

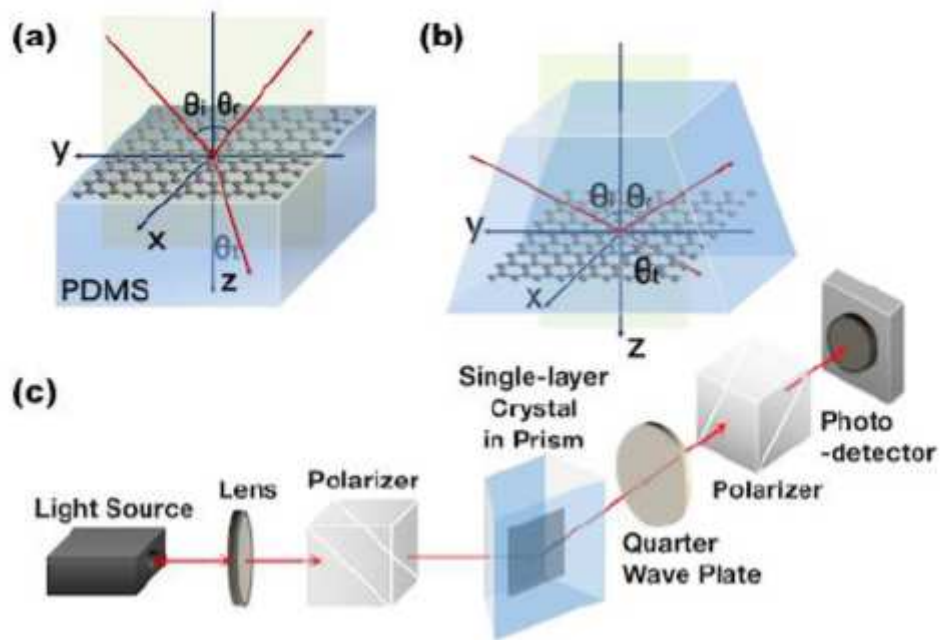
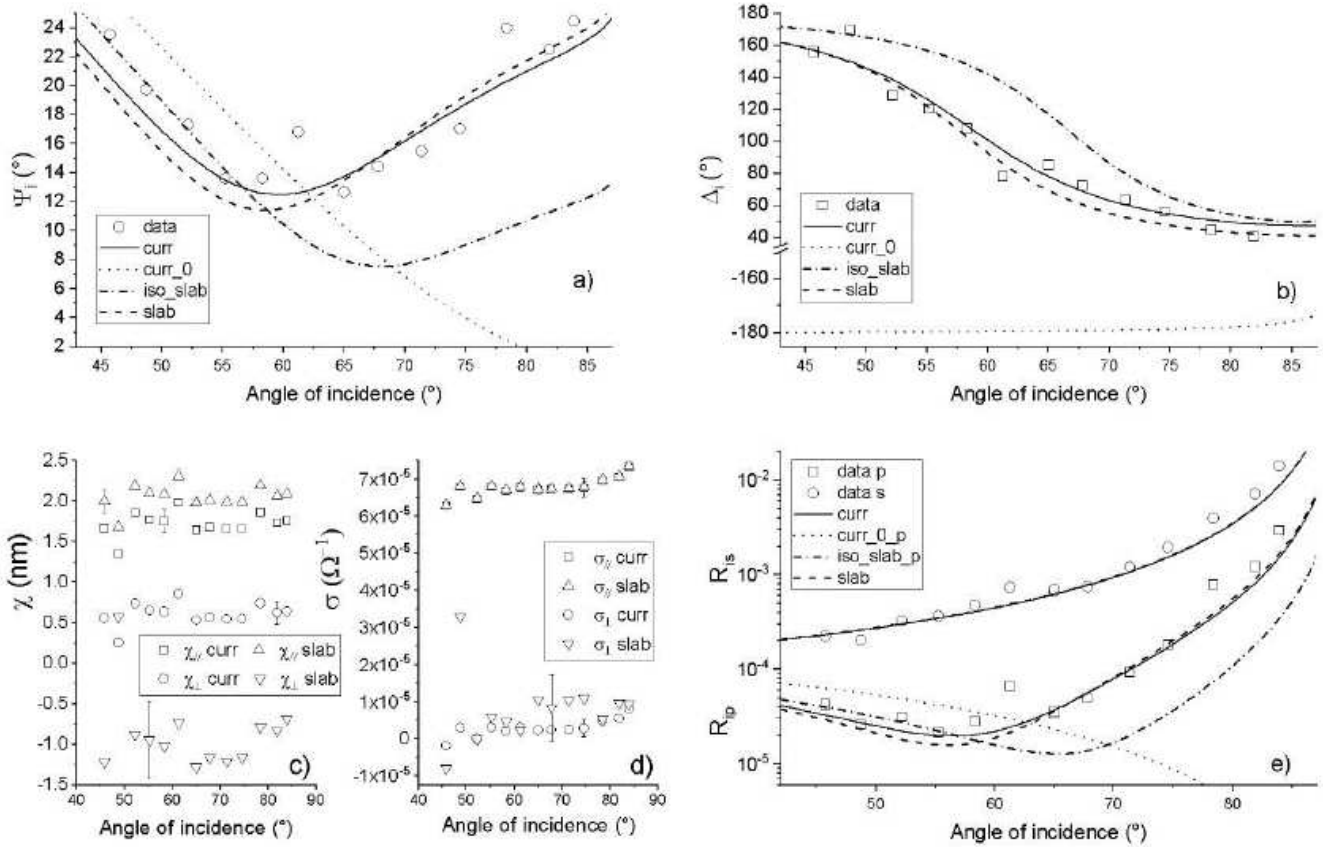


Figure 1

Experimental set up. a, scheme of the standard spectroscopic ellipsometry on a single-layer 2D crystal deposited on a PDMS substrate. b, scheme of the manual ellipsometric measurement on the same crystal completely immersed in a PDMS prism. c, set up of the manual ellipsometer, at the wavelength of 633 nm.



**Figure 2**

See manuscript for full figure caption.

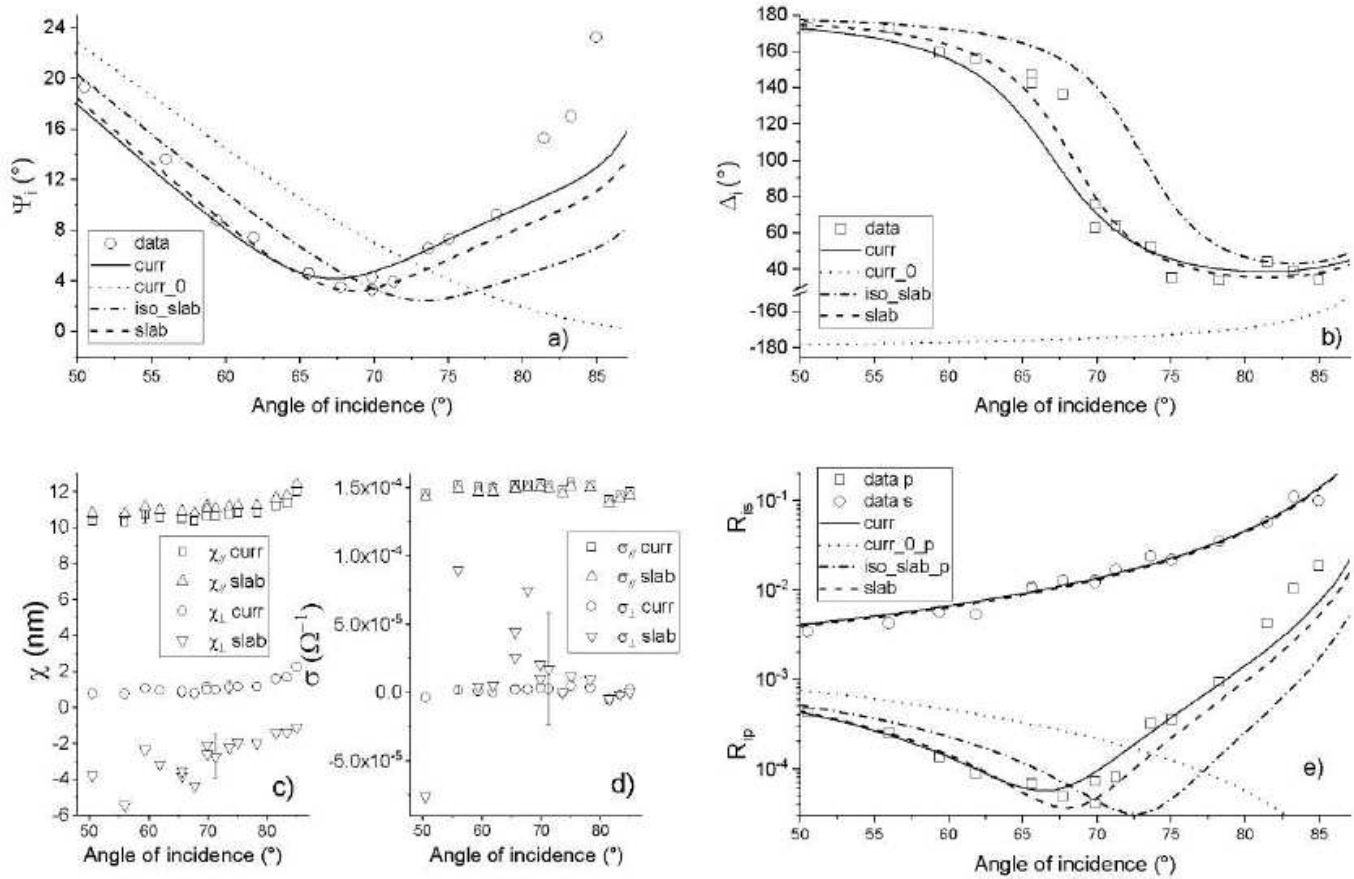


**Figure 3**

See manuscript for full figure caption.